Indian Journal of Chemical Technology
Vol. 32, November 2025, pp. 766-777
DOI: 10.56042/ijct.v32i6.16791

Impacts of both the pressure work and activation energy on electro-osmotic flow of Eyring-Powell nanofluid

H. A. Sayed[1*], M. Y. Abouzeid[2] & S. A. Hussein[1]

[1]Department of Mathematics, Faculty of Science, Zagazig University, Zagazig, Egypt

[2]Department of Mathematics, Faculty of Education, Ain Shams University, Heliopolis, Cairo, Egypt

*E-mail: haahmmad@science.zu.edu.eg

Received 30 January 2025; accepted 16 May 2025

This study focuses on the electro-osmotic flow of Eyring–Powell nanofluids through a non-Darcy porous medium, incorporating the effects of time-periodic variations. A comprehensive mathematical model is developed, considering key physical influences such as activation energy, pressure work, Hall currents, mixed convection, thermal radiation, electro-osmosis, viscous dissipation, Ohmic heating, and diffusion-thermo effects. Mass momentum, energy and nanoparticles concentration conservation principles are used to formulate the governing partial differential equations that are nonlinear which have been resolved by the explicit method of finite differences. A set of figures are presented to elucidate the impact of the problem's physical factors on the solutions found. In addition, the Sherwood number, Nusselt number, and skin friction coefficient are computed. An upsurge in Gebhart number and thermodynamic Rayleigh number lower both the fluid velocity and temperature while raising the nanoparticles concentration. Moreover, the increase in dimensionless Helmholtz–Smoluchowski velocity and Darcy number lead to a rise in Nusselt number while lowering the Sherwood number and skin friction coefficient. The importance of this kind of research therefore comes from its prospective applications in industry and biomedical engineering, as it may be utilized to dewater sediments and liquids from human tissues that are infected.

Keywords: Activation energy, Eyring-Powel nanofluid, Hall currents, Pressure work, Zadunaisky‘s method

Introduction

Recently, the importance of fluids for increasing heat transport in many engineering structures, such as flood defense and fuel cells has attracted many researchers. However, to address this topic, we focus on high-thermal conductivity fluids because of their ability to transfer heat. The mixture of a base fluid with nanometer-sized particles is called nanofluid. The usage of nanofluids in the storage systems of thermal energy causes both solar power plants and heat pumps to operate more effectively. Choi and Eastman introduced the idea of nanofluid for the first time[1]. Bhatti *et al.* [2] used Keller-Box method to obtain a numerical solution for the action of uniform magnetic field on hybrid nanofluid flow. The MHD convection heat transport of hybrid nanofluid has been studied experimentally and numerically by Narankhishig *et al.*[3]. The MHD pulsatile Newtonian nanofluid circulation in a wavy channel with radiation and a heat source was examined by Dawood *et al.*[4]. The electroosmotic micropolar non-Newtonian nanofluid flow along an endless vertical surface with ohmic and viscous dissipation componentsis discussed by Abouzeid and Shaaban[5]. Ouaf and Abouzeid[6] analyzed the action of radially varying viscosity on Newtonian nanofluid transport through a non-Darcy porous media. The effects of both Ohmic heating and variable thermal conductivity on non-Newtonian nanofluid flow past a moving surface of variable thickness are explored by Eldabe et al.[7]. Abouzeid and Ibrahim[8] utilized the multi-step differential transform method for treating the problem of both activation energy and Hall current impacts on MHD mixed convection non-Newtonian nanofluid flow. In order to gain significant knowledge for magnetic drug delivery, intelligent lubrication, and heat management systems, Sharma and Kumar[9] examined the impacts of low-frequency oscillation magnetic fields, nanoparticle dimension impacts, and nanolayer dynamics on ferrofluid flow across an upward/downward moving revolving disc. Taking into account the impacts of viscous dissipation, Sharma *et al.*[10] examined the flow and heat transmission properties of water-copper (Cu/H_2O) nanofluids over a spinning disc moving uphill or downhill. In order to provide insights for utilization in

heating and cooling and rotating machinery systems, they examined the effects of nanoparticle concentration, disc rotation, and vertical motion on velocity profiles, distribution of temperatures, and thermal performance. Other researchers have also explained the nature and application of nanofluid on different surfaces[11-22].

Recently, research on the flow of non-Newtonian nanofluids in boundary layers under the influence of electroosmotic forces has attracted significant attention. When the bulk liquid moves through a narrow tube due to the effect of an external electric field along the tube axis, an electrokinetic phenomenon is induced, known as electroosmosis. If the tube wall carries a negative charge, it attracts cations from the electrolyte solution and repels anions, thereby forming an electric double layer (EDL). Ahmed *et al.*[23] discussed the electro osmosis and mixed convection action on Non-Newtonian nanofluid circulation across a non-Darcy porous medium. The influence of both chemical reaction and activation energy on electro-osmotic flow of the boundary layer of a micropolar Williamson nanofluid was examined by Hegazy *et al.*[23]. Hafez et al. [24] examined viscous and Joule dissipations impacts on Casson nanofluid on a stretched sheet with electroosmosis force present. A mathematical model for the electroosmotic flow of viscoelastic fluids has been investigated by Herrera-Valencia *et al.*[25]. Banerjee and Pati[26] studied the problem of two immiscible fluids flow in a microchannel with the effects of both electro-osmosis and pressure driven. There are some other research pertaining to the electro-osmosis nanofluids flow through various shapes that can be observed via studies[27-30].

According to the literature reviewed thus far and ongoing research, no effort has been made to examine how Hall and time-periodic fluctuations affect Eyring-Powell nanofluid movement in a porous material that isn't Darcy with linear thermal radiation. No attempt has been made to develop a model that integrates Zadunaisky's technique on the impact of pressure work and Hall currents on electro-osmotic flux of non-Newtonian nanofluids.

In the present work, the solutions for the Eyring-Powell nanofluid flow affected by diffusion-thermo, electro-osmosis, viscous, and Ohmic dissipation effects are examined, along with the activation energy suggested by Arrhenius. This paper investigates electro-osmotic nanofluid flow without Newtonian motion past an endless vertical surface. Numerous cutting-edge components contribute to this research study's uniqueness and significance. The following summarizes this study's distinctive contribution:

- The impact of the rmodynamic Rayleigh numbers on velocity and temperature distribution.
- How skin friction and the distribution of velocity are affected by electro-osmosis factors.
- The behavior of temperature and nanoparticles concentration is based on the thermophoresis parameter and Gebhart number.
- How momentum and the Sherwood number are affected by the dimensionless chemical interaction parameter.
- Using the capabilities of Zadunaisky's technique, a new numerical computation methodology is presented to examine how Eyring-Powell nanofluid circulation in a non-Darcy porous material is affected by Hall electricity and electromagnetic hydrodynamics.
- The efficiency of Zadunaisky ‘s method in justifying the use of estimated answers as an appropriate approximation for physical values that have been calculated.

Formulation of problem

Consider the unstable two-dimensional structures flow through the boundary layer of mechanical heat transfer Powell-Eyring fluid along an infinite vertical plate, as illustrated in Fig. 1. This scenario includes flow over a non-Darcy porous media. The mathematical framework incorporates the equation for continuity (Eq. 1) as well as the momentum conservation equations, energy, and nanoparticles concentration (Eqs 2-4) that govern fluid flow behaviour. It is important to look at the theories of Maxwell and Ohm's laws during this visualization.

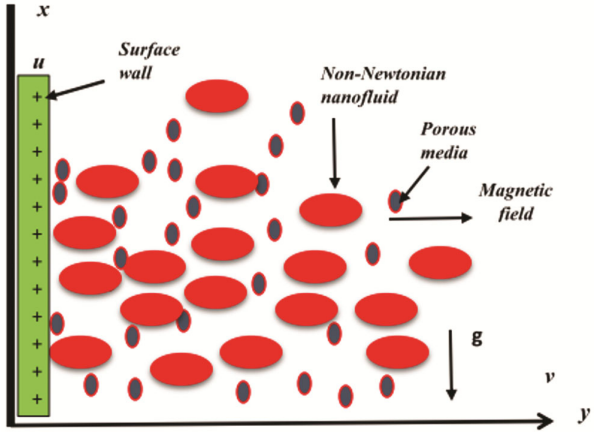

Fig. 1 — Sketch of the problem

Heat transportation is analyzed using Joule heating, viscous dispersion, the pressure work, linear radiation, mixed convection and heat source. In addition, pressure work and activation energy are considered. Furthermore, Powell-Eyring nanofluid model incorporates the impact of Hall current. In this case, the fluids are electrically conducting, and the Powell-Eyring nanofluids are impacted by the Hall current that is generated at higher magnetic field intensities. The problem's governing equations are provided as[23].

$$\frac{\partial u}{\partial x}+\frac{\partial v}{\partial y}=0 \qquad \text{... (1)}$$

$$\frac{\partial u}{\partial t}= -\frac{1}{\rho}\frac{\partial p}{\partial x}+\nu\frac{\partial^2 u}{\partial y^2}+\frac{1}{\rho a b}\left(\frac{\partial^2 u}{\partial y^2}\right)\frac{1}{\sqrt{\frac{1}{a^2}\left(\frac{\partial u}{\partial y}\right)^2+1}}-\left(\frac{\sigma B_0^2}{\rho(1+m^2)}+\frac{\nu}{K}\right)u-\bar{b}u^2+\rho_e E_x+ g_0\overline{\beta}(T-T_\infty)+g_0\overline{\beta}^*(C-C_\infty) \qquad \text{... (2)}$$

$$\frac{\partial T}{\partial t}=\frac{k}{\rho C_p}\frac{\partial^2 T}{\partial y^2}+\frac{\nu}{C_p}\left(\frac{\partial u}{\partial y}\right)^2+ \frac{1}{\rho b C_p}\left(\frac{\partial u}{\partial y}\right)\sinh^{-1}\left(\frac{1}{a}\frac{\partial u}{\partial y}\right)+\nabla\cdot\underline{q}+\frac{\sigma B_0^2}{\rho C_p(1+m^2)}u^2+ +D_B\left(\frac{\partial T}{\partial y}\frac{\partial C}{\partial y}\right)+D_T\left(\frac{\partial T}{\partial y}\right)^2\frac{D_B K_T}{C_p C_s}\frac{\partial^2 C}{\partial y^2}+\overline{\beta}T\left(u\frac{\partial p}{\partial x}\right)+Q_0(T-T_\infty) \qquad \text{... (3)}$$

$$\frac{\partial C}{\partial t}=D_B\frac{\partial^2 C}{\partial y^2}+\frac{D_T}{T_m}\frac{\partial^2 T}{\partial y^2}-\lambda_0\left(\frac{T}{T_\infty}\right)^{\bar{n}}e^{-\frac{E_a}{k^* T}}\left(C-C_\infty\right) \qquad \text{... (4)}$$

Considering the beginning and boundary circumstances [23]:

$$u=0,\quad T=T_\infty,\quad C=C_\infty \quad for\,all\quad t\le 0 \qquad \text{... (5-a)}$$

$$u=0,\quad T=T_\infty+\varepsilon(T_\omega-T_\infty)\cos\omega t,\quad C=C_\infty+\varepsilon(C_\omega-C_\infty)\cos\omega t \quad at\ y=0,\quad t>0 \qquad \text{... (5-b)}$$

$$u\to 0,\ T\to T_\infty,\ C\to C_\infty \ \text{ as }\ y\to\infty,\ t>0 \qquad \text{... (5-c)}$$

By applying both consequence of Rosseland approximation and Taylor series[31], the divergence of radiated thermal flux can be characterized as:

$$\nabla\cdot\underline{q}=\frac{-16\sigma^*}{3k_R}\frac{\partial^2 T}{\partial y^2} \qquad \text{... (6)}$$

By applying Gaussian's theory [18,32], we acquire:

$$\overline{\varepsilon}\left(\nabla\cdot\underline{E}\right)=\rho_e\ . \qquad \text{... (7)}$$

Being a conservative field, the electric field [32], then:

$$\overline{\varepsilon}\nabla^2\varphi=-\rho_e \qquad \text{... (8)}$$

$$\rho_e=-Z_\nu e(n^- -n^+) \qquad \text{... (9)}$$

$$n^{\pm}=n_0\, e^{\mp\frac{e\,z_\nu}{k_B T_{av}}\varphi} \qquad \text{... (10)}$$

with the net charge number density calculated as[32]: By using Debye–Huckel linearization principle $\frac{e\,z_\nu}{k_B T_{av}}=1$, in, Eq. (9), we obtain

$$\rho_e=-\frac{\overline{\varepsilon}}{\lambda_e{}^2}\varphi \qquad \text{... (11)}$$

$$\lambda_e=\frac{1}{e\,z_\nu}\sqrt{\frac{\overline{\varepsilon}k_B T_{av}}{2n_0}} \qquad \text{... (12)}$$

By applying boundary-layer approximations, Eq. (8) can be written as[18,32]:

$$\frac{d^2\varphi}{dy^2}=\frac{1}{\lambda_e{}^2}\varphi \qquad \text{... (13)}$$

Let us introduce the subsequent dimensionless variables[23]:

$$t^*=\frac{t}{t_m},\ \omega^*=t_m\,\omega,\ y^*=\frac{y}{L_m},\ u^*=\frac{u}{u_m},\ p^*=\frac{t_m}{\mu}p,\quad T^*=\frac{T-T_\infty}{T_\omega-T_\infty},\ C^*=\frac{C-C_\infty}{C_\omega-C_\infty},\quad \varphi^*=\frac{\varphi}{\xi},\ \beta=\frac{T_\omega}{T_\infty} \qquad \text{... (14)}$$

where $u_m=(\nu g_0\overline{\beta}\Delta T)^{\frac{1}{3}}$, $L_m=\left(\frac{g_0\overline{\beta}\Delta T}{\nu^2}\right)^{-\frac{1}{3}}$, and

$$t_m=(g_0\vec{\beta}\Delta T)^{-\frac{2}{3}}\nu^{\frac{1}{3}} \qquad \text{... (15)}$$

Now, Eq. (13) may be written as[32]:

$$\frac{d^2\varphi}{dy^2}=m_e{}^2\,\varphi \qquad \text{... (16)}$$

We consider the boundary conditions $\varphi(0) = 1$ and $\varphi(\infty) \to 0$, to obtain a solution of Eq. (16) as follows:[18,32]:

$$\varphi = e^{-m_e y} \quad \text{... (17)}$$

Then, the set of equations obtained by applying the dimensionless entities presented in Eq. (14) is provided by, following the removal of the star symbol:

$$\frac{\partial u}{\partial t} = \left(1 + \frac{\hat{\alpha}}{\sqrt{\gamma\left(\frac{\partial u}{\partial y}\right)^2 + 1}}\right)$$

$$\frac{\partial^2 u}{\partial y^2} - \left(\frac{Ha^2}{1+M^2} + \frac{1}{Da}\right)u - Fs\,u^2 + U_{HS}\, m_e^{\,2}\, e^{-m_e y} + T + N\,C \quad \text{... (18)}$$

$$\frac{\partial T}{\partial t} = \frac{(3+4R)}{3\,\mathrm{Pr}}\frac{\partial^2 T}{\partial y^2} + Ec\left(\frac{\partial u}{\partial y}\right)^2 + \frac{Ec}{\delta}\left(\frac{\partial u}{\partial y}\right)\sinh^{-1}\left(\sqrt{\gamma}\frac{\partial u}{\partial y}\right) + M\,Ec\,u^2 + Q_0\,T + D_f\frac{\partial^2 C}{\partial y^2} + Nb\left(\frac{\partial T}{\partial y}\frac{\partial C}{\partial y}\right) + Nt\left(\frac{\partial T}{\partial y}\right)^2 - Ge\,\mathrm{Re}\,(T+\Lambda)\,u \quad \text{... (19)}$$

$$\frac{\partial C}{\partial t} = \frac{1}{Sc}\frac{\partial^2 C}{\partial y^2} + \frac{Nt}{Nb}\frac{\partial^2 T}{\partial y^2} - k_\alpha\left(1+\left(\bar{\beta}-1\right)T\right)^{\bar{n}} e^{\left(\frac{E_A}{1+(\beta-1)T}\right)} C \quad \text{... (20)}$$

$u = 0, \quad T=0, C=0 \qquad$ for all y, t ≤ 0 ... (21-a)

$u = 0, T=\varepsilon\cos\omega t, C=\varepsilon\cos\omega t$ at y=0, t > 0 ... (21-b)

$u\to 0, \quad T\to 0, \quad C\to 0 \quad$ as $\quad y\to\infty$, t > 0 ... (21-c)

By using both Taylor expansion and the assumption $(\beta-1)<<1$, Eq. (19) becomes

$$\frac{\partial C}{\partial t} = \frac{1}{Sc}\frac{\partial^2 C}{\partial y^2} + \frac{Nt}{Nb}\frac{\partial^2 T}{\partial y^2} - k_\alpha\, e^{-E_A}\left(1+\left(\bar{n}+E_A\right)\left(\bar{\beta}-1\right)T\right) C \quad \text{... (22)}$$

Approach to the solution

Method of finite differences

The system of Eqs (18), (19) and (22) considering those boundary constraints (21a-c), they are solved numerically utilizing the finite difference method[16]. Therefore, Eqs (18), (19) and (22) can be written as:

$$\frac{u_i^{n+1}-u_i^n}{\Delta\tau} - \left(\frac{u_{i+1}^n - 2u_i^n + u_{i-1}^n}{(\Delta y)^2}\right)\left(\hat{\alpha}\Big/\sqrt{\gamma\left(\frac{u_{i+1}^n-u_i^n}{\Delta y}\right)^2+1}\right) - Fs\left(u_i^n\right)^2 + \left(\frac{Ha^2}{1+M^2}+\frac{1}{D_a}\right)u_i^n + U_{HS}\, m_e^{\,2}\, e^{-m_e i\Delta y} - T_i^n - N\,C_i^n = 0 \quad \text{... (23)}$$

$$\frac{T_i^{n+1}-T_i^n}{\Delta\tau} - \frac{(3+4R)}{3\,\mathrm{Pr}}\left(\frac{T_{i+1}^n - 2T_i^n + T_{i-1}^n}{(\Delta y)^2}\right) - Ec\left(\frac{u_{i+1}^n-u_i^n}{\Delta y}\right)^2 - \frac{E_c}{\delta}\left(\frac{u_{i+1}^n-u_i^n}{\Delta y}\right)\times \sinh^{-1}\left(\sqrt{\gamma}\left(\frac{u_{i+1}^n-u_i^n}{\Delta y}\right)\right) - MEc\,(u_i^n)^2 - Q_0\,T_i^n - Nb\left(\frac{T_{i+1}^n-T_i^n}{\Delta y}\times\frac{C_{i+1}^n-C_i^n}{\Delta y}\right) - Nt\left(\frac{T_{i+1}^n-T_i^n}{\Delta y}\right)^2 - D_f\left(\frac{C_{i+1}^n-2C_i^n+C_{i-1}^n}{(\Delta y)^2}\right) + Ge\,\mathrm{Re}\left(T_i^n+\Lambda\right)u_i^n = 0 \quad \text{... (24)}$$

$$\frac{C_i^{n+1}-C_i^n}{\Delta\tau} - \frac{1}{Sc}\left(\frac{C_{i+1}^n-2C_i^n+C_{i-1}^n}{(\Delta y)^2}\right) - \frac{Nt}{Nb}\left(\frac{T_{i+1}^n-2T_i^n+T_{i-1}^n}{(\Delta y)^2}\right) + k_\alpha\, e^{-E_A}\left(1+\left(\bar{n}+E_A\right)\left(\bar{\beta}-1\right)T_i^n\right)C_i^n = 0 \quad \text{... (25)}$$

where y and t are denoted by the indexes i and n, correspondingly, with Δy= h=0.04 and $\Delta\tau$=0.002. Mathematica package is used to solve the algebraic Eqs (23)-(25) numerically with the boundary conditions (21a-c), subsequently a Newton-Raphson iterative technique determines the velocity, the temperature, and concentration of the nanoparticles to be a function of y and proceeds until whether the accuracy objective or the precision goal are reached.

Global error estimation

Zadunaisky 's method[33] is used to compute the estimation of global error. His idea could be elucidated in the subsequent steps:

It is possible to interpolate the values u_i^n, T_i^n and C_i^n, where (i=1,2,….., 21). Then, we give them names P_i (i=1,2,…..,21). Furthermore, after interpolating the values u", T" and C", identify them by their names $R_1(y)=u$", $R_2(y)=T$", $R_3(y)=C$".

1) We compute the identify functionalities d_i (i=1,2,…..,21)as follows:
   $d_1(y)= P_1' - P_2 = 0$, $d_2(y)= P_2' - R_1(y)$,
   $d_3(y)= P_3' - P_4 = 0$, $d_4(y)= P_4' - R_2(y)$,
   $d_5(y)= P_5' - P_6 = 0$, $d_6(y)= P_6' - R_3(y)$,
2) Adding these determine functionalities d_i (i=1,2,…..,21) addressed the initial issues and name the new solution z_i (i=1,2,…..,21).

3) The new answer Z(z), whose elements are z_i (i=1,2,…..,21), is obtained by solving the dummy issue using the finite difference methodology.
4) Calculating the estimation of global errors using e_i=Zi-P(z_i), (i=1,2,...,21), wherein Z(z_i) represents the accurate solution of the pseudo-problem at z_n and z_i represents the closest possible solution of the pseudo-problem at z_i. Clearly, we imagine that Z(z_n)= P(z_n) is the precise answer to the pseudo-problem.
5) The global values for errors are acquired and summarized as indicated in Table 1. The basis for this inaccuracy is the use of 21 points to determine the degree of the applying interpolation to polynomial PI (I=1, 2,... 6). [20,33].

Sherwood, Nusselt, and skin friction numbers

The non-dimensional form of the skin-friction coefficient involving heat and mass transmission is as follows:

$$\tau_\omega = \left[\frac{\partial u}{\partial y}\left(1+\frac{\alpha}{\sqrt{\gamma\left(\frac{\partial u}{\partial y}\right)^2+1}}\right)\right]_{y=0} \quad \text{... (26)}$$

$$Nu = -\left(\frac{\partial T}{\partial y}\right)_{y=0} \quad \text{... (27)}$$

$$Sh = -\left(\frac{\partial C}{\partial y}\right)_{y=0} \quad \text{... (28)}$$

Results and Discussion

The analysis of the influence of the various problem variables, which is shown in Figs. (2)–(22), validated the conclusions that were achieved. Furthermore, it is believed that the non-dimensional parameters have the ones that follow fixed values:

ω= 0.01, $t = 0.1\,\pi, \gamma = 0.4$, ε=0.05, $\alpha = 0.3, M = 1, Da = 0.1, Fs = 0.5, Gr = 0.5, Pr = 2.5, Q = 5, Ec = 1, Sc = 1, Df = 0.01, Nb = 2.5, Nt = 3.5$, $m_e = 0.1$, $U_{HS} = 2$, R=1, $k_0 = 0.1$, n=2, $\beta = 1.02, E_A = 0.01$, Ge=4, Re=0.4, $\Lambda = 1.4$.

Hall[34] first discovered the concept of Hall current. The result of a potential variation that runs counter to an electric current flowing within a conductor of electricity is known as Hall action. The Hall current parameter is the ratio of the magnetic field that is generated to the combination of the current density and the produced electric field. Since its value depends on the range of charges and their types, it is always a distinctive attribute of the material. Figs 2 and 3 display the action of the dimensionless velocity of Helmholtz-Smoluchowski U_{HS} and Hartmann Number Ha on the distribution of velocity u, respectively. There is evidence that the acceleration

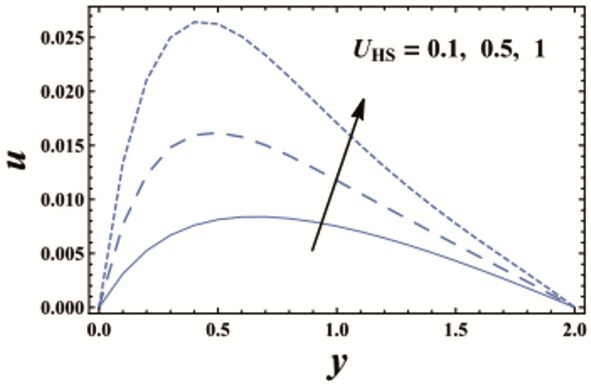

Fig. 2 — Velocity profile for U_{HS}

Table 1 — Estimation of the global errors for temperature, velocity, and concentration of nanoparticles

y	u	e_1	T	e_3	C	e_5
0	0	0	0.05	0	0.05	0
0.2	0. 005399	0.200D-3	0.090910	0.1800D-4	0.012517	−0.4300D-6
0.4	0. 007874	0.100D-2	0.117415	0.1200D-3	−0.008571	−0.2500D-6
0.6	0.009740	0.170D-3	0.130125	0.4100D-3	−0.016760	−0.2100D-5
0.8	0.008655	0.530D-3	0.130801	0.8000D-4	−0.008571	−0.1400D-4
1	0.008456	0.700D-2	0.121790	0.2300D-3	−0.016300	−0.8000D-5
1.2	0.007962	0.110D-3	0.105522	0.5600D-3	−0.005719	−0.8900D-6
1.4	0.006847	0.120D-2	0.084115	0.6200D-4	−0.001625	−0.2900D-4
1.6	0.003764	0.410D-2	0.059074	0.1600D-3	−0.000128	−0.5300D-4
1.8	0.001940	0.160D-3	0.031097	0.3200D-3	−0.000490	−0.2600D-4
2	0	0	0	0	0	0

distribution rises as values of U_{HS} increase, but it falls as *Ha* rises. Furthermore, as the dimensionless coordinate y increases the highest value that can be found for *u* for each value of both U_{HS} and *Ha*, increases, but when *Ha* rises, it falls. The top of this paragraph explains the result in Fig. 3. The outcome in Fig. 2 is explained as follows: it is well-known that any solution containing electric field charges creates a force called Coulomb force. Electro-osmotic flow is caused by Coulomb force. The Debye layer is an accumulation of mobile ions that forms in the area close to the interface since the chemical equilibrium involving the surface as well as a solution of electrolytes often causes the interface to acquire an overall fixed charge of electricity. The ensuing Coulomb force causes the overall charge in the electrically charged double layer to move once an electrical field is introduced to the fluid. Electro-osmotic flow is the name given to the resultant flow. Thus, a greater resultant Coulomb force facilitates fluid movement. The interaction between the acceleration distribution u and the dimensionless chemical response constant k_α is depicted in Fig. 4. With the exception of the generated curves overlapping close to the surface wall, it is discovered that the impact of U_{HS} on u is identical to the impact of k_α on u, namely, in the interval $y \in [0.0, 0.2]$. Fig. 5 illustrates how the Schmidt number *Sc* affects the velocity distribution u. It is shown that the behavior of u for different values of Sc in the interval of coordinate $y \in [0.0, 1.11]$ is precisely the same as the behaviour of u for different values of *Ha* in Fig. 3. Additionally, it is shown in Fig. 5 that the curves are extremely close to one another within the range of the axial coordinate $y \in [1.11, \infty)$. Additionally, the highest possible value of u persists at y = 0.67 in the very initial interval, and this optimum value slowly declines as the overall value of *Sc* increases.

The Figs 6 and 7, illustrate how the temperature distribution T changes when considering the dimensionless coordinates y for various amounts of the thermophoresis coefficient *Nt* and Gebhart number *Ge*, respectively. As the parameter *Nt* increases, the temperature gradient T rises, according to the graphical results in Figs 6 and 7, whereas it decreases as Ge increases. Now, the result in Fig. 6 will be explained; from a physical point of view; Thermophoresis also known as thermo-migration or thermo-diffusion, is a phenomenon that occurs in a blend of mobile particles exhibiting different

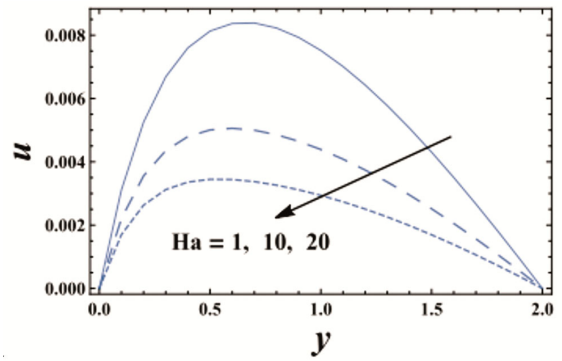

Fig. 3 — Velocity profile for *Ha*

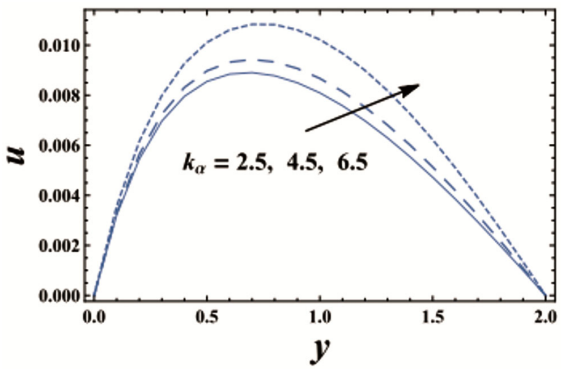

Fig. 4 — Velocity profile for k_α

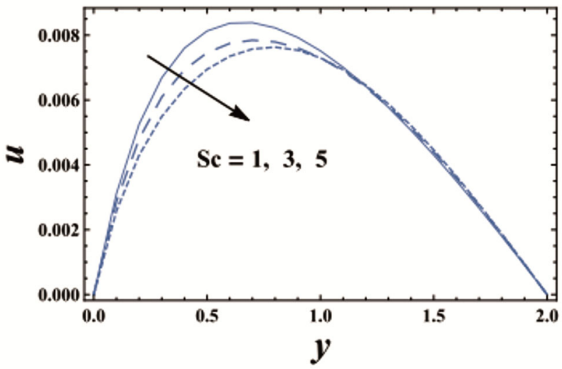

Fig. 5 — Velocity profile for *Sc*

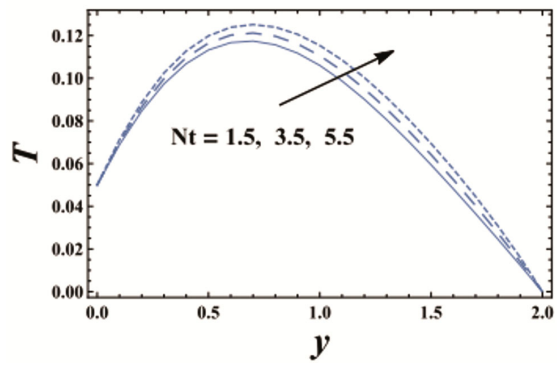

Fig. 6 — Temperature profile for *Nt*

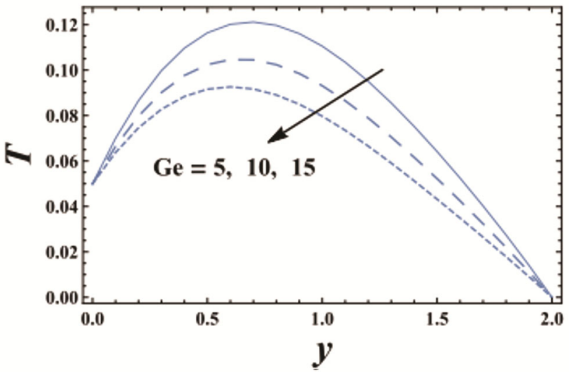

Fig. 7 — Temperature profile for *Ge*

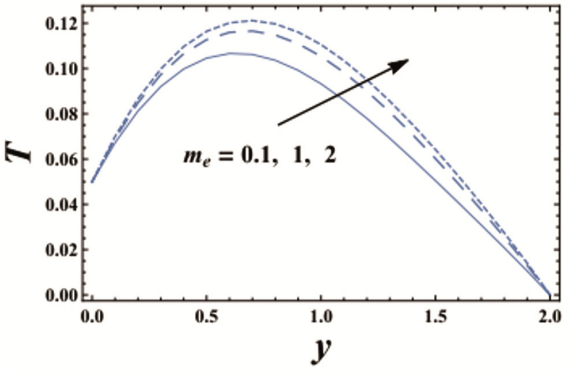

Fig. 9 — Temperature profile for m_e

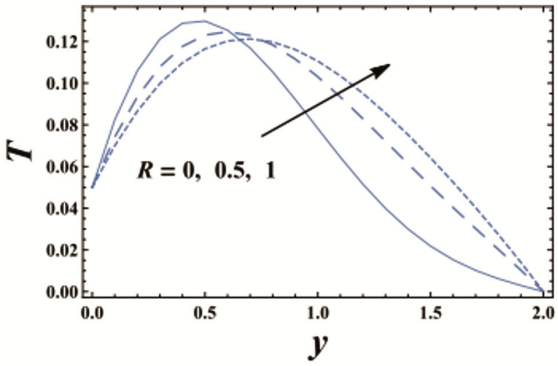

Fig. 8 — Temperature profile for *R*

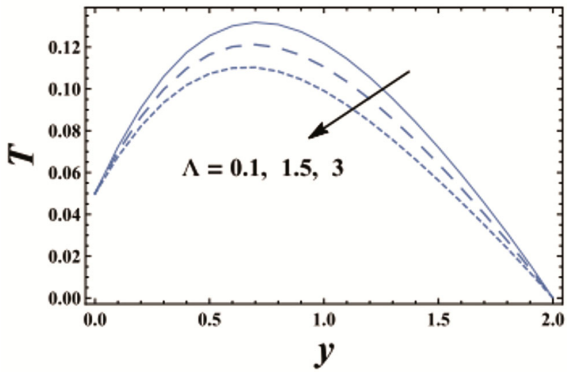

Fig. 10 — Temperature profile for Λ

responses to the temperature gradient force. It controls the transfer of molecules along a temperature gradient. The particles subjected to the bombardment of higher energy molecules will have a higher temperature. Consequently, this explains the result in Fig. 6. This conduct is consistent with what has been reported[35,36]. Additionally, it is noted that T rises with y until a certain value, $y=y_0$, which denotes the highest value of T, and then falls. Fig. 8 shows how the thermal distribution T is affected by the radiation level parameter R. It is discovered that the thermal distribution T decreases with an increase in R throughout intervals $y \in [0.0, 0.67]$, otherwise it increases with increasing *R*. T behaves differently in the range of $y \in [0.67]$, than it does in the remainder of the intervals. There exist maximum values of T for every value of R within the first interval, and these values decrease as R rises. Figs (9) and (10) elucidate the variation impacts of the electroosmotic parameter m_e and the thermodynamic Rayleigh number **Λ** on the temperature distribution T, respectively. As seen in Figs 9 and 10, except for the fact that the curves are much larger than those shown in Figs 6 and 7, the curves' behavior is comparable to that found in those figures. The following outcomes seen in Fig. 10 are caused by the thermodynamic Rayleigh number defined as the strength of thermal buoyancy thermodynamic to viscous and thermal diffusion. It is inversely proportional to the energy generated from both viscous dissipation and Soret effect leading to a decrease in temperature.

The random movement of nanoparticles immersed in a media, which could be a liquid or a gas, is known as Brownian motion in physics. Typically, this motion pattern involves a particle moving to a different sub-domain after experiencing random oscillations in its current location within a fluid sub-domain. The newly established closed volume undergoes further variations after each migration. This pattern increases the concentration of nanoparticles and characterizes a liquid at thermal equilibrium. This will clarify the subsequent outcome. The distribution of the concentration of the nanoparticle C with the dimensionless direction y is shown in Figs 11 and 12 for varying values of the parameter for thermophoresis *Nt* and the Brownian motion parameter *Nb*, correspondingly. As can be observed from these figures, the concentration of nanoparticles rises with increasing *Nb* values while falling with increasing *Nt*. The nanoparticles concentration

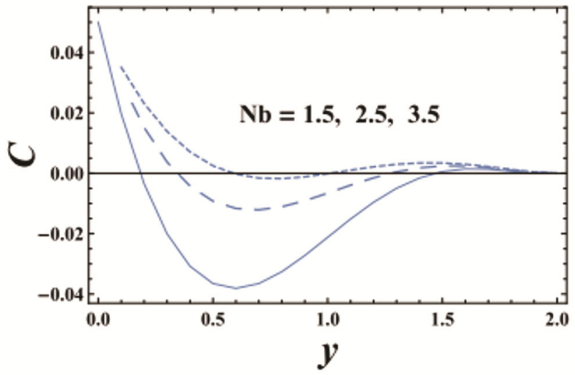

Fig. 11 — Nanoparticles concentration profile for *Nb*

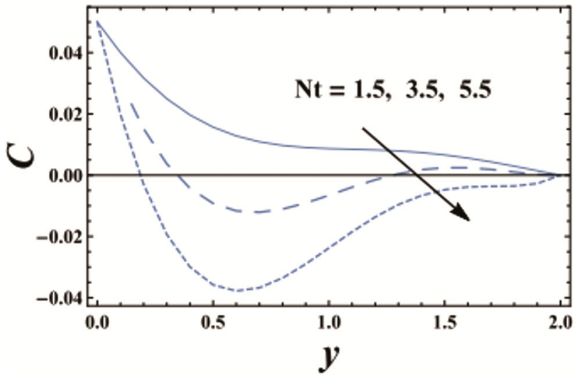

Fig. 12 — Nanoparticles concentration profile for *Nt*

distribution C of the nanoparticles for small values of *Nb* as well as high values of *Nt* decreases as the coordinate *y* increases, reaching a minimum value before increasing. The effect of the Dufour number D_f on the nanoparticles concentration distribution C as determined by the value of dimensionless coordinate y is shown in Fig. 13. It is evident that the behavior of C for different values of D_f in the range associated with the coordinate y [0.0, 1.3] is exactly the same as the behavior of C for different values of Nt shown in Fig. 12; otherwise, the produced curves overlap. In the starting interval, C has the smallest value at y = 0.62 for every value of the factor D_f. The distribution of the concentration of nanoparticles C is shown in Fig. 14, which shows the effect of the dimensionless chemical interaction constant k_α. It is observed that the influence of k_α on *C* is the reverse of the influence of D_f on *C*, as seen in Fig. 13. The only difference is that the curves' behaviour with y is wavy for small quantities of k_α, but they resemble a parabolic shape with a minimum value for large values of k_α. Other parameters' effects are comparable to those seen in Figs 11–14. To conserve space, some figures are not included here.

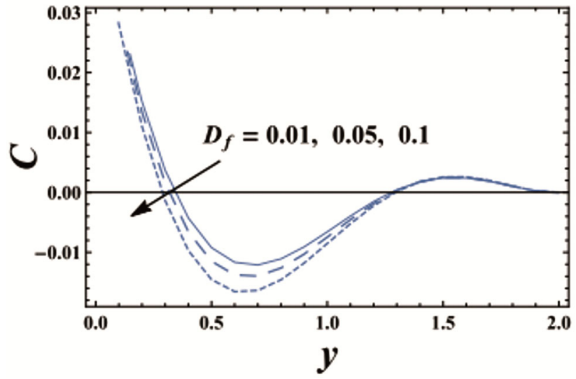

Fig. 13 — Nanoparticles concentration profile for D_f

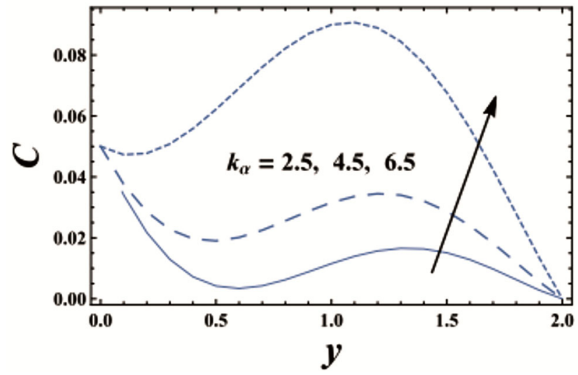

Fig. 14 — Nanoparticles concentration profile for $\mathbf{k_\alpha}$

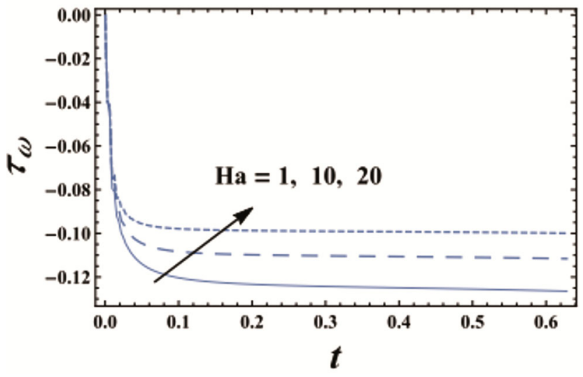

Fig. 15 — Skin friction profile for *Ha*

The behaviour of the skin coefficient of friction with time *t* for different values of the dimensionless Helmholtz-Smoluchowski velocity and Hartmann number *Ha* is depicted in Figs 15 and 16. These figures illustrate that as *Ha* increases, the skin friction factor also increases, and conversely, when *Ha* decreases, the skin friction coefficient decreases as well. Furthermore, Figs 15 and 16 show that the skin coefficient of friction initially becomes negative and decreases with increasing *t* until it reaches a finite value, at which point it remains relatively constant over time.

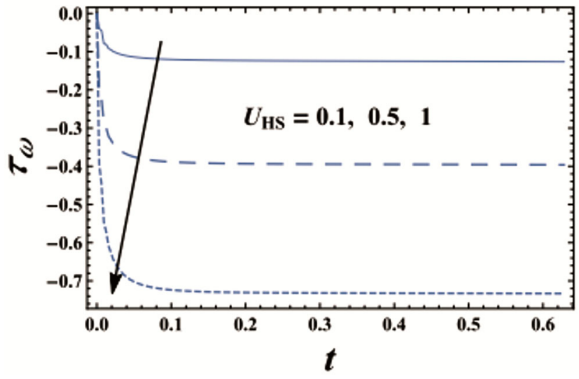

Fig. 16 — Skin friction profile for U_{HS}

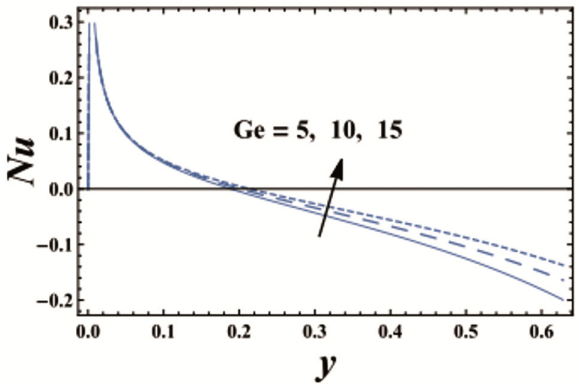

Fig. 17 — Nusselt number profile for *Ge*

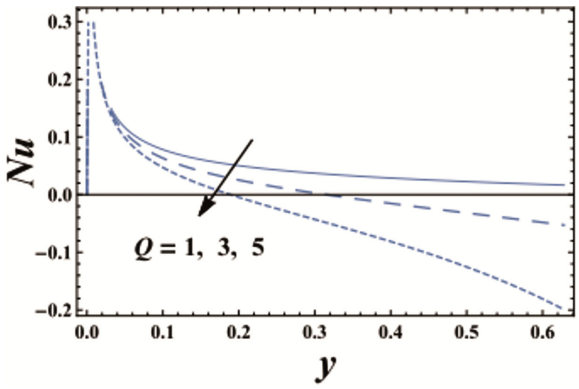

Fig. 18 — Nusselt number profile for *Q*

Figs 17 and 18 show Nusselt number *Nu* values plotted against time *t* for different Gebhart number *Ge* values and the parameter of heat source *Q* values. These figures illustrate that *Nu* increases with *Ge* and decreases with *Q*. Additionally, *Nu* values for various *Ge* and *Q* values initially increase with time tuntil reaching a finite value, after which they decrease. Fig. 19 demonstrates how *Nu* changes with *y* for various radiation parameter *R* values. *Nu* decreases as *R* approaches the outermost wall y ∈ [0, 0.21], as shown in Fig. 19; elsewhere, it increases as *R*

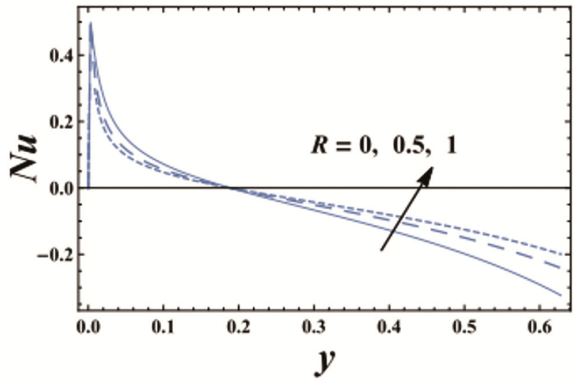

Fig. 19 — Nusselt number profile for *R*

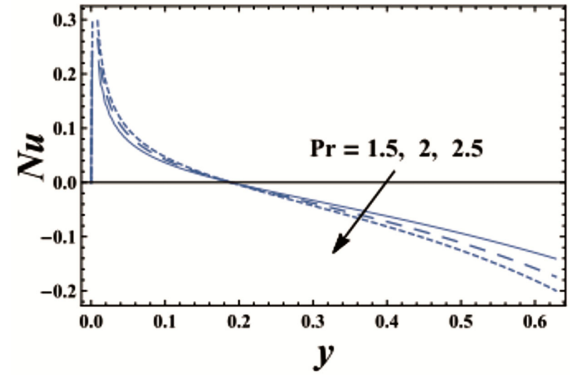

Fig. 20 — Nusselt number profile for *Pr*

increases. This indicates a different behaviour of *Nu* in the region r ∈ [0.21, ∞] compared to y∈ [0, 0.21]. In Fig. 20, the relationship between Prandtl number *Pr* and the *Nu* is shown. The lines in Fig. 20 are closer together compared to Fig. 19, suggesting that the influence of *Pr* on *Nu* is opposite to the impact of *R* on *Nu* as shown in Fig.19. Due to space constraints, additional figures are not included here as their results are consistent with those in Figs 17 and 18.

For various values of the amplitude ratio ε and the dimensions chemical reaction parameter k_α, the behaviour of the Sherwood coefficient *Sh* with time *t* is shown in Figs 21 and 22, correspondingly. The amplitude ratio increases *Sh* value, whereas the dimensionless chemical reaction parameter decreases it, as illustrated by these figures. Additionally, it is observed that the values of *Sh* is always positive, that the difference between the *Sh* for various values of ε , and that k_α is reduced as *t* grows and approaches a minimum value before increasing. As ε increases, the absolute minimum value of *Sh* rises, but when k_α increases, it falls.

Table 2 presents numerical results for the skin friction τ_ω, reduced Nusselt number *Nu* and Sherwood

Table 2 — Comparison of the physical quantities of present study with those obtained by Ahmed et al.[23]

ε	Pr	Q_0	τ_ω in the present study	τ_ω (Ahmed *et al.*[23])	Nu in the present study	Nu (Ahmed *et al.*[23])	Sh in the present study	Sh (Ahmed *et al.*[23])
0.05	2.5	1	0.0805	0.0797	-0.0026	-0.0024	0.0059	0.0066
0.1	2.5	1	0.1705	0.1816	-0.0088	-0.0083	0.0780	0.0821
0.2	2.5	1	0.5812	0.6342	-0.2003	-0.1749	0.6005	0.5998
0.2	3	1	0.3008	0.2951	-0.0301	-0.0221	0.1804	0.2042
0.2	3.5	1	0.3110	0.2954	-0.0392	-0.0320	0.1930	0.2166
0.2	4	1	0.3190	0.2957	-0.0510	-0.0424	0.2089	0.2297
0.2	4	2	0.2306	0.2290	-0.2407	-0.2348	0.3948	0.4089
0.2	4	3	0.2988	0.3047	-0.6016	-0.5515	0.7004	0.6691
0.2	4	4	0.3089	0.3169	-0.9899	-1.1642	0.9960	1.1732

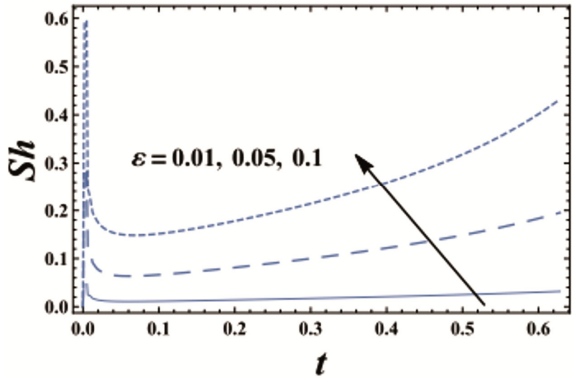

Fig. 21 — Sherwood number profile for ε

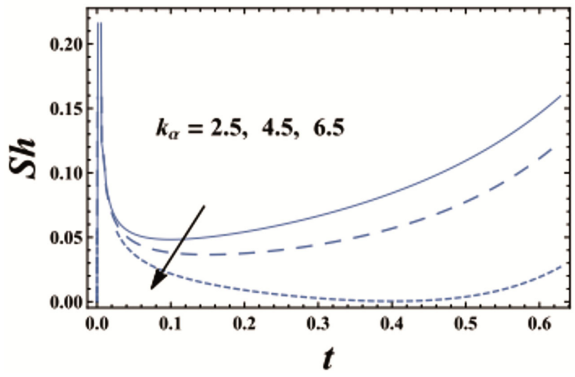

Fig. 22 — Sherwood number profile for k_α

number *Sh*, for various values of the wave amplitude ε, Prandtl number Pr and heat source parameter Q_0. It is clear from Table 2, that an increase in ε, Pr and Q_0 gives an increase in the values of dimensionless quantity τ_ω and *Sh*, but decreasing in the dimensionless quantity *Nu*. In addition, these results have been compared with those obtained by B´eg et al.[42], and it is found that there is a good agreement between our results and those of Ahmed et al.[23].

Conclusion

The adapted Eyring-Powel nanofluid flow electroosmosis problem on a sheet that is stretching has been addressed. Mixed convection, thermal radiation, pressure work, heat source, activation energy, Ohmic, and viscous dissipation all have an impact on the flow through a porous non-Darcy medium. An explicit finite differences approach has been used to solve a predefined entire set of nonlinear differential equations with partial differentials. Additionally, the Zadunaisky technique is utilized to estimate the error rate for the scheme in question. As a sufficient approximation to the computed physical values, the estimated errors contain the approximated solutions. It is intended that this work would help people grasp more complicated issues in engineering, industry, and some physiological flows[37-39]. Graphs have been used to examine the impact of the various parameters on these flow variables. The present analysis yields the following main findings:

- ❖ Higher values of dimensionless Helmholtz–Smoluchowski velocity, the dimensionless chemical reaction parameter and Brownian motion parameter enhance the velocity, whereas Hall current parameter, Schmidt number and thermodynamic Rayleigh number drop the velocity.
- ❖ Both dimensionless Helmholtz–Smoluchowski velocity, thermodynamic Rayleigh number and Gebhart number lower the temperature profile, while it rises as both the electroosmotic parameter, the thermophoresis parameter and the Brownian motion parameter rise.
- ❖ As y increases, the temperature rises for various issue parameter values until it reaches a maximum value.
- ❖ Regarding the behaviour of temperature, the concentration of nanoparticles exhibits the opposite behaviour.
- ❖ The skin-friction drops with increasing dimensionless Helmholtz–Smoluchowski velocity, Darcy number and heat source parameter,

however it rises due to the increment of Hall current parameterand of the electroosmotic parameter.

- ❖ An upsurge in Prandtl number and Reynolds number increase or decrease both Nusselt number and Sherwood number.
- ❖ The Nusselt number rises, and the Sherwood number falls as the Gebhart and Schmidt numbers rise.

Parametric study could be expanded in future studies to investigate how other fluid characteristics, such as the morphologies of nanoparticles, affect the dynamics of flow. A stability analysis of the flow and an investigation of the nonlinear effects may offer a more profound understanding of the system's behaviour in harsh environments, which is crucial for high-performance industrial applications. Experimental research should be done to support theoretical conclusions, with a particular emphasis on practical uses like thermal energy storage devices and MHD generators.

Conflict of interest

The authors declare no conflict of interest.

References

1 Choi S U & Eastman J A, Enhancing thermal conductivity of fluids with nanoparticles, (Argonne National Lab, (ANL), Argonne, IL (United States), (1995).

2 Bhatti M M, Öztop H F & Ellahi R, Study of the magnetized hybrid nanofluid flow through a flat elastic surface with applications in solar energy, *Materials*, 15 (2022) 7507.

3 Narankhishig Z, Ham J, Lee H & Cho H, Convective heat transfer characteristics of nanofluids including the magnetic effect on heat transfer enhancement-A review, *Appl Therm Eng*, 193 (2021) 116987.

4 Dawood A, Kroush F A, Abumandour R M & Eldesoky I M, Pulsatile nanofluid flow with variable pressure gradient and heat transfer in wavy channel, *Sci Rep*, 14 (2024) 9351.

5 Abouzeid M & Shaaban A, Electroosmotic flow of micropolar nanofluid through a non-Darcy porous media with Von Neumann stability condition, *Spec Top Rev Porous Media*, 16 (2025) 21.

6 Ouaf M E & Abouzeid M, Chemically reacted blood CuO nanofluid flow through a non-Darcy porous media with radially varying viscosity, *Sci Rep*, 14 (2024) 1650.

7 Eldabe N, Abouzeid M, Seliem A A, Elanna A & Hegazy N, Variable thickness with Ohmic heating and viscous dissipation effect on MHD Casson-nanofluid flow through a porous media, *Indian J Chem Technol*, 31 (2024) 613.

8 Abouzeid M & Ibrahim M, Multi-step differential transform method for both Hall currents and mixed convection effects on MHD flow of non-Newtonian fluid with Al_2O_3 nanoparticles, *Egypt J Chem*, 67 (2024) 225.

9 Sharma K & Kumar S, Impacts of low oscillating magnetic field on ferrofluid flow over upward/downward moving rotating disk with effects of nanoparticle diameter and nanolayer, *J Magn Magn Mater*, 575 (2023) 170720.

10 Sharma K, Kumar S & Vijay N, Insight into the motion of water-copper nanoparticles over a rotating disk moving upward/downward with viscous dissipation, *Int J Mod Phys B*, 36 (2022) 2250210.

11 Abdelmoneim M, Eldabe N, Abouzeid M & Ouaf M, Electro-osmotic effect on the peristaltic flow of Williamson nanofluid through a porous medium in the presence of activation energy and modified Darcy's law, *Indian J Chem Technol*, 31 (2024) 257.

12 Abouzeid M & Ibrahim M, Both micro-structural slips and conductivity variation properties of magneto nanoflow of micropolar fluid, *Egyp J Chem*, 67 (2024) 273.

13 Abuiyada A J, Eldabe N T, Abou-Zeid M Y & El-Shaboury S M, Activation energy and couple stresses effect on MHD peristaltic transport of jeffery nanofluid between two inclined coaxial tubes through a Non-Darcy porous medium, *J Appl Nonlinear Dyn*, 13 (2024) 705.

14 Mohamed Y M, El-Dabe N T, Abou-Zeid M Y, Mostapha D R & Oauf M E, Impacts of hall and ion slip currents with cattaneo-christov features on the peristaltic blood flow of sisko micropolar nanofluid inside an annulus through a porous medium, *J Appl Nonlinear Dyn*, 13 (2024) 735.

15 Eldabe N T, Abou-Zeid M Y, El-Shabouri S M & Ismael A M, Both radially varying viscosity and thermal micropolar effect on MHD Newtonian nanofluid flow through a porous media, *Int J Ambient Energy*, 45 (2024) 2367737.

16 Abou-Zeid M & Sayed H, Impacts of thermal conductivity and viscosity variation parameters on non-Newtonian nanofluid flow with mixed convection and chemical reaction features, *Int J Ambient Energy*, 45 (2024) 2367114.

17 Eldabe N, Abouzeid M, Abdelmoneim M & Ouaf M, Impacts of activation energy and electroosmosis on peristaltic motion of micropolar Newtonian nanofluid inside a microchannel, *Mod Phys Lett B*, 39 (2024) 2450407.

18 Eldabe N T, Hussein S A, Gabr M E & Zaher A Z, A novel mathematical model of MHD boundary layer flow of an activated micropolar nanofluid over a stretching surface under the effect of electro-osmosis forces, *Mod Phys Lett B*, 37 (2023) 2350153.

19 Hussein S A & Eldabe N T, Peristaltic transport of radiative and dissipative MHD third order nanofluid through the vertical asymmetric channel with heat and mass convection, *Int J Ambient Energy*, 45 (2024) 2266435.

20 Ahmed S E, Arafa A A & Hussein S A, Hydrothermal dissipative nanofluid flow over a stretching riga plate with heat and mass transmission and shape effects, *J Therm Anal Calorim*, 149 (2024) 4855.

21 Nagy M, Hussein S A & Mansi A, Fourth-grade nanofluid model with dissipative and nonlinear radiative properties transported peristaltically via a flexible diverging duct holding a porous media under the influence of concentration and heat convection in an induced magnetic field, *Numer Heat Transf Part A: Appl*, (2024) 1.

22 Eldabe N, Gabr M & Hussein S A, Numerical treatment for the boundary layer flow of Sutterby nanofluid through porous medium with planktonic microorganisms over a stretching Riga cylindrical tube, *Int J Ambient Energy*, 45 (2024) 2345251.

23 Ahmed O, Eldabe N, Abou-Zeid M, El-Kalaawy O & Moawad S, Numerical treatment and global error estimation

for thermal electro-osmosis effect on non-Newtonian nanofluid flow with time periodic variations, *Sci Rep*, 13 (2023) 14788.

24 Hafez N, Thabet E N, Khan Z, Abd-Alla A & Elhag S, Electroosmosis-modulated Darcy-Forchheimer flow of Casson nanofluid over stretching sheets in the presence of Newtonian heating, *Case Stud Therm Eng*, 53 (2024) 103806.

25 Herrera-Valencia E, Sánchez-Villavicencio M L, Soriano-Correa C, Bautista O, Ramírez-Torres L A, Hernández-Abad V J & Calderas F, Study of the electroosmotic flow of a structured fluid with a new generalized rheological model, *Rheol Acta*, 63 (2024) 3.

26 Banerjee D, Pati S & Biswas P, Analytical study of two-layered mixed electro-osmotic and pressure-driven flow and heat transfer in a microchannel with hydrodynamic slippage and asymmetric wall heating, *Phys Fluids*, 34 (2022) 032013.

27 Hegazy N, Eldabe N T, Abouzeid M, Abousaleem A & Alana A, Influence of both chemical reaction and electro-osmosis on MHD non-Newtonian fluid flow with gold nanoparticles, *Egypt J Chem*, 66 (2023) 191.

28 Eldabe N, Abouzeid M, Abdelmoneim M & Ouaf M E, Electro-osmotic peristaltic flow of non-Newtonian nanofluid Al_2O_3 inside a microchannel with modified Darcy's law and activation energy, *Egypt J Chem*, 67 (2024) 251.

29 Abdelmoneim M, Eldabe N, Abouzeid M & Ouaf M, Electro-osmotic peristaltic flow of non-Newtonian Sutterby TiO_2 nanofluid inside a microchannel through porous medium with modified Darcy's law, *Mod Phys Lett B*, 38 (2024) 2450239.

30 Abdelmoneim M, Eldabe N T, Abouzeid M Y & Ouaf M E, Modified Darcy's law and couple stress effects on electro-osmotic flow of non-Newtonian nanofluid with peristalsis, *Int J Appl Electrom Mech*, 72 (2023) 253.

31 Ghoneim M E, Khan Z, Zuhra S, Ali A & Tag-Eldin E, Numerical solution of Rosseland's radiative and magnetic field effects for Cu-Kerosene and Cu-water nanofluids of Darcy-Forchheimer flow through squeezing motion, *Alex Eng J*, 64 (2023) 191.

32 Nadeem S, Kiani M N, Saleem A & Issakhov A, Microvascular blood flow with heat transfer in a wavy channel having electroosmotic effects, *Electrophoresis*, 41 (2020) 1198.

33 Aïd R & Levacher L, Numerical investigations on global error estimation for ordinary differential equations, *J Comput Appl Math*, 82 (1997) 21.

34 Hall E H, On a new action of the magnet on electric currents, *Am J Math*, 2 (1879) 287.

35 Ahmed S E, Arafa A A & Hussein S A, Viscous dissipation and Joule heating in case of variable electrical conductivity Carreau-Yasuda nanofluid flow in a complex wavy asymmetric channel through porous media, *Mod Phys Lett B*, 38 (2024) 2450369.

36 Shah Z, Islam S, Gul T, Bonyah E & Khan M A, The electrical MHD and hall current impact on micropolar nanofluid flow between rotating parallel plates, *Results Phys*, 9 (2018) 1201.

37 Xu Y J, Nazeer M, Hussain F, Khan M I, Hameed M K, Shah N A & Chung J D, Electro-osmotic flow of biological fluid in divergent channel: Drug therapy in compressed capillaries, *Sci Rep*, 11 (2021) 23652.

38 Alyousef H A, Yasmin H, Shah R, Shah N A, El-Sherif L S & El-Tantawy S A, Mathematical modeling and analysis of the steady electro-osmotic flow of two immiscible fluids: A biomedical application, *Coatings*, 13 (2023) 115.

39 Al-Griffi T A J & Ali-Al-Saif A S J, An approach for computational blood flow under the joint effects of the electro-osmotic, magnetic field, chemical reaction and porosity, *Eng Comput*, 40 (2023) 1851.